

Terahertz quantum Hall effect for spin-split heavy-hole gases in strained Ge quantum wells

This content has been downloaded from IOPscience. Please scroll down to see the full text.

2016 New J. Phys. 18 113036

(<http://iopscience.iop.org/1367-2630/18/11/113036>)

View [the table of contents for this issue](#), or go to the [journal homepage](#) for more

Download details:

IP Address: 217.112.157.113

This content was downloaded on 25/11/2016 at 18:25

Please note that [terms and conditions apply](#).

You may also be interested in:

[Terahertz spectroscopy of quantum 2D electron systems](#)

James Lloyd-Hughes

[Magnetotransport properties of 2D fermionic systems with k-cubic Rashba spin–orbit interaction](#)

Alestin Mawrie, Tutul Biswas and Tarun Kanti Ghosh

[Landau levels and Shubnikov–de Haas oscillations in monolayer transition metal dichalcogenide semiconductors](#)

Andor Kormányos, Péter Rakyta and Guido Burkard

[Quantum oscillations and interference effects in strained n- and p-type modulation doped GaInNAs/GaAs quantum wells](#)

F Sarcan, F Nutku, O Donmez et al.

[Defect-induced overshoot of quantum Hall plateaus](#)

Qin Wang, H Q Xu, P Omling et al.

[A review of the electrical properties of semiconductor nanowires: Insights gained from terahertz conductivity spectroscopy](#)

Hannah J Joyce, Jessica L Boland, Christopher L Davies et al.



OPEN ACCESS

RECEIVED
20 July 2016REVISED
24 October 2016ACCEPTED FOR PUBLICATION
27 October 2016PUBLISHED
21 November 2016Original content from this
work may be used under
the terms of the [Creative
Commons Attribution 3.0
licence](#).Any further distribution of
this work must maintain
attribution to the
author(s) and the title of
the work, journal citation
and DOI.

PAPER

Terahertz quantum Hall effect for spin-split heavy-hole gases in strained Ge quantum wells

M Failla¹, J Keller², G Scalari², C Maissen², J Faist², C Reichl³, W Wegscheider³, O J Newell¹, D R Leadley¹,
M Myronov¹ and J Lloyd-Hughes¹¹ University of Warwick, Department of Physics, Gibbet Hill Road, Coventry, CV4 7AL, UK² Institute for Quantum Electronics, ETH Zürich, 8093 Zürich, Switzerland³ Laboratory for Solid State Physics, ETH Zürich, 8093 Zürich, SwitzerlandE-mail: j.lloyd-hughes@warwick.ac.uk**Keywords:** terahertz, quantum Hall effect, germanium, spin-orbit, strain, quantum well

Abstract

Spin-split heavy-hole gases in strained germanium quantum wells were characterized by polarisation-resolved terahertz time-domain spectroscopy. Effective masses, carrier densities, g-factors, transport lifetimes, mobilities and Rashba spin-splitting energies were evaluated, giving quantitative insights into the influence of strain. The Rashba coefficient was found to lower for samples with higher biaxial compressive strain, while heavy-hole mobilities were enhanced to over $1.5 \times 10^6 \text{ cm}^2 \text{ V}^{-1} \text{ s}^{-1}$ at 3 K. This high mobility enabled the observation of the optical quantum Hall effect at terahertz frequencies for spin-split two-dimensional heavy-holes, evidenced as plateaux in the transverse magnetoconductivity at even and odd filling factors.

Introduction

The spin-orbit interaction (SOI) gives rise to fascinating physical phenomena, and offers potential application in spintronic devices as it can lift spin degeneracy even at zero external magnetic field [1]. The SOI can arise from bulk or structural inversion asymmetries (BIA or SIA, respectively). The SIA is particularly interesting as it can be provided in modulation-doped heterostructures, and can be controlled by applying an external electric field or by changing the doping density. Two-dimensional hole gases (2DHGs) in strained Ge quantum wells (sGe-QWs) are attractive systems for spintronics due to their compatibility with CMOS technology and finite SO effects, driven by the Rashba SOI [2–4]. Furthermore, as mobilities can approach or exceed $10^6 \text{ cm}^2 \text{ V}^{-1} \text{ s}^{-1}$ in strained Ge [5, 6], exotic many-body effects such as the quantum Hall effect (QHE) [3] and the fractional QHE [7, 8] have been observed in a dc electric field.

In Ge quantum wells with $\text{Si}_{1-x}\text{Ge}_x$ buffer layers the degeneracy of the heavy hole (HH) and light hole (LH) valence bands is lifted by strain, giving an energy difference $E_{\text{HH,LH}} = |E_{\text{HH}} - E_{\text{LH}}|$ at zero wavevector [9, 10], and making HHs lighter. The Rashba SOI further lifts the degeneracy of HHs and LHs, [2, 11] giving spin-split states even at zero magnetic field B , with an energy that depends on odd-powers of the in-plane wavevector k . As opposed to the k -linear Rashba SOI experienced by conduction band electrons and LHs, for HHs the Rashba SOI contributes with a k -cubic dependence, leading to a different effective magnetic field. The energy difference between spin-up and spin-down states is $\Delta = 2\beta k_F^3$, where β is the cubic Rashba coefficient, $k_F = \sqrt{2\pi\rho_{2D}}$ is the Fermi wavevector, and ρ_{2D} is the carrier sheet density. Since $\beta \propto 1/(E_{\text{HH,LH}})^2$, strain also plays an important role in determining properties for spintronic applications [2].

Intriguingly, recent years have shown an ac analogue of the QHE when a dc magnetic field B and the ac electric field of light are perpendicular: the optical quantum Hall effect (OQHE). A numerical study of the dynamical response [12] predicted plateaux-like features in the transverse (off-diagonal) magnetoconductivity $\sigma_{xy}(\omega, B)$ at THz frequencies, at integer values of the filling factor $\nu = h\rho_{2D}/eB$. Experimentally, plateaux in $\sigma_{xy}(\omega)$ or in the Faraday rotation angle have been witnessed only for electrons in GaAs heterostructures [13, 14] or for Dirac fermions in graphene [15]. In this project we established and investigated the physics of the OQHE

for HHs in strained germanium. Important distinctions about this system in comparison to previous studies are that: (i) the Rashba SOI can contribute in sGe, whereas it is negligible in the OQHE systems reported so far [13–15], (ii) the Zeeman energy $m_j g^* \mu_B B$ is larger for HHs (which have magnetic quantum number $m_j = \pm 3/2$) than for electrons ($m_j = \pm 1/2$) for the same effective g -factor g^* , (iii) the strength of the Rashba energy Δ and Zeeman energy are closely linked to the strain, and (iv) the valence band structure of sGe is more strongly non-parabolic than that of the GaAs conduction band.

In this work we used polarisation-resolved THz time-domain spectroscopy (THz-TDS) to study high mobility 2DHGs in sGe-QWs in the quantum Hall regime. A comparison with a GaAs/AlGaAs 2DEG permitted HHs to be uniquely identified by the ellipticity of the transmitted THz radiation. In contrast to our previous work, which examined the longitudinal conductivity of lower mobility samples with lower strain [4], here we report strain-enhanced lifetimes with mobilities exceeding $1.5 \times 10^6 \text{ cm}^2 \text{ V}^{-1} \text{ s}^{-1}$. The study of $\sigma_{xy}(\omega, B)$ from the complex Faraday spectra allowed the direct observation of the OQHE for 2D HHs, via distinct plateaux in σ_{xy} near integer filling factors. A qualitative difference between samples with different well thicknesses is the presence or absence of plateaux at odd ν . This difference is linked to the contrasting Landau fan dispersions that result from different g -factors. The width of the OQHE plateaux for 2DHGs is compared with literature results for GaAs/AlGaAs 2DEGs. An experimental oscillation in the cyclotron resonance width with magnetic field is ascribed to the changing Landau level (LL) occupancy, as suggested by a model of the joint density of states (JDOS). Finally, the enhanced strain lowers the Rashba interaction strength Δ as a consequence of an increased HH–LH splitting energy.

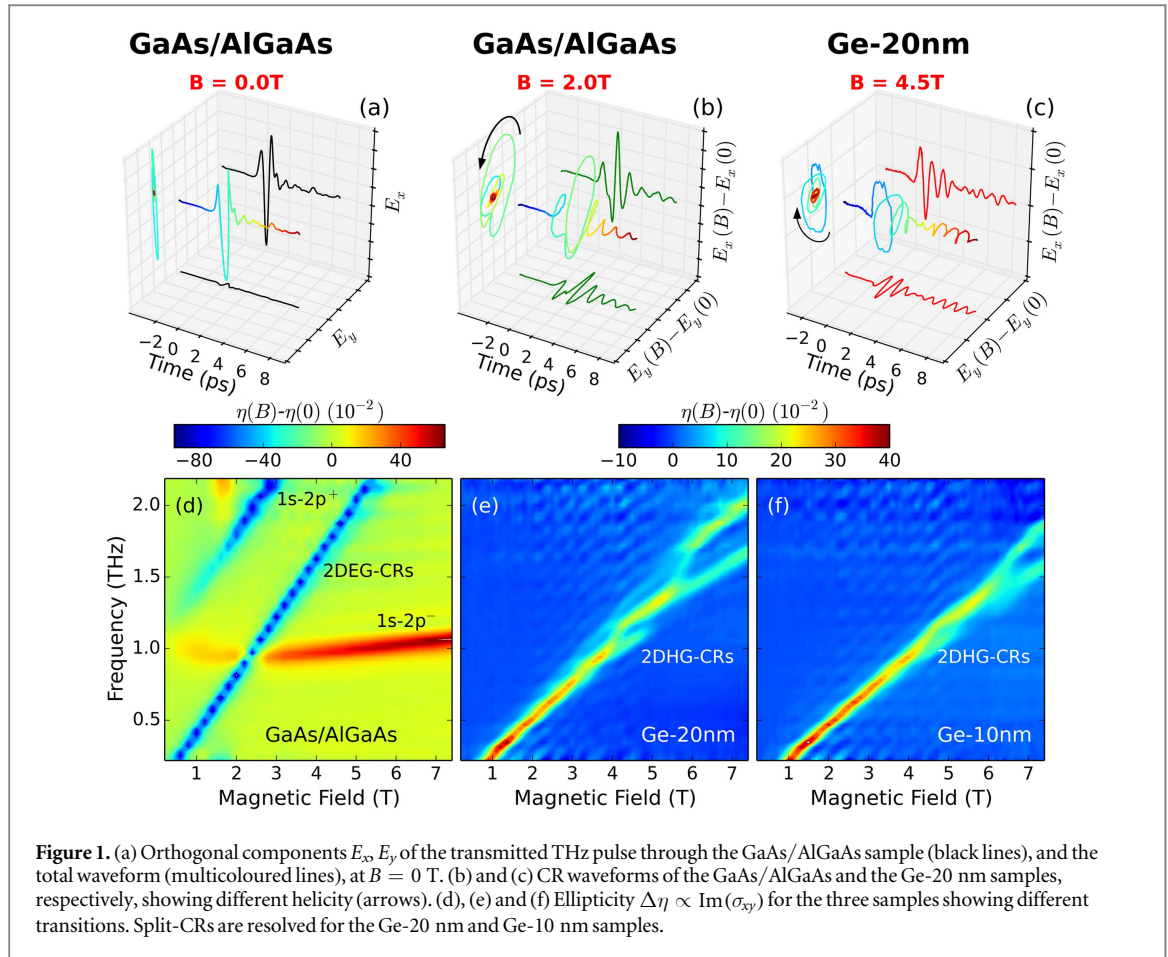
Experimental method

Modulation-doped $\text{Si}_{0.3}\text{Ge}_{0.7}/\text{Ge}/\text{Si}_{0.3}\text{Ge}_{0.7}$ heterostructures were grown using an ASM Epsilon 2000 RC-CVD reactor, with 1.3% in-plane compressive strain [6]. Samples are labelled as Ge-10nm and Ge-20 nm, in accordance with the thickness of each Ge QW. Holes are supplied by a boron-doped SiGe layer (dopant density $2 \times 10^{18} \text{ cm}^{-3}$). The low doping ensures that only the HH subband is occupied. Details of the GaAs/AlGaAs sample ($4 \times 30 \text{ nm}$ QWs) can be found in [16]. Polarisation-resolved THz-TDS was performed by generating linearly polarised THz pulses using an interdigitated GaAs emitter photoexcited by femtosecond pulses from a Ti:sapphire laser oscillator. A wire grid polariser was placed after the THz emitter. THz pulses were focused on samples placed in a superconducting magnet in the Faraday geometry, where $B = 0.0 - 7.5 \text{ T}$ was applied along the growth axis in 0.1 T steps, and at $T = 3 \text{ K}$. To investigate the longitudinal and transverse response of HHs to an ac electric field, the orthogonal components of the THz radiation were probed using electro-optic sampling with a (111)-oriented ZnTe crystal [17, 18]. This directly yields the complex transverse conductivity $\sigma_{xy}(\omega, B)$ (Hall response) and longitudinal conductivity $\sigma_{xx}(\omega, B)$.

In figure 1(a) the x - and y -components ($E_x \gg E_y$) of the transmitted THz pulse through the GaAs/AlGaAs sample at $B = 0 \text{ T}$ are shown in the time domain. For 2D electronic systems under a magnetic field CR absorption arises from transitions between occupied LLs $|N\rangle$ and unoccupied LLs $|N + 1\rangle$. The selection rule is such that there are cyclotron resonance active (CRA) and inactive (CRI) modes E_{\pm} , where \pm denote right and left-handed light. Under an applied magnetic field the Faraday effect alters the amplitude, phase and polarisation of the transmitted THz pulse because of the different absorption coefficients and refractive indices of the CRA and CRI modes E_{\pm} [19].

The CR response can be resolved in the time domain by subtracting the transmitted THz electric field at $B = 0 \text{ T}$ from that at finite B , i.e. $E_{x,y}^{\text{CR}}(B, t) = E_{x,y}(B, t) - E_{x,y}(0, t)$. Examples of the CR response in the time domain for the GaAs/AlGaAs and the Ge-20 nm samples are given in figures 1(b) and (c). Beating effects are clearly visible in E_x^{CR} and E_y^{CR} , as a consequence of multiple transitions with different frequencies [4]. In contrast to our previous work [4], which just examined E_x^{CR} , the additional knowledge of E_y^{CR} allows the definitive identification of the type of quasiparticle undergoing CR. The total CR-waveforms $E^{\text{CR}}(t) = E_x^{\text{CR}} \hat{x} + E_y^{\text{CR}} \hat{y}$, shown as multicoloured lines in figures 1(b) and (c), are elliptically polarised with opposite helicity (arrows) for the 2DEG and the 2DHG. This is because the CRA modes for electrons are CRI for holes, as a consequence of the opposite sense of cyclotron rotation due to the opposite sign in the effective mass [20].

The time-domain data were Fourier transformed, and then converted to a circular basis set using $E_{\pm}(B) = \sqrt{1/2} (E_x(B) \pm iE_y(B))$. This then permits the real and imaginary components of the complex Faraday angle [21] $\Theta_F(\omega, B) = \theta_F(\omega, B) + i\eta(\omega, B)$ to be found. The transmitted pulse is rotated by the Faraday angle $\theta_F = (\arg(E_+) - \arg(E_-))/2$, while the ellipticity is $\eta = (|E_+| - |E_-|)/(|E_+| + |E_-|)$ [22]. To rule out any contribution to θ_F and η at $B = 0 \text{ T}$ due to the small but finite ellipticity of the incident pulse (figure 1(a)), we considered $\Delta\theta_F = \theta_F(B) - \theta_F(B = 0)$ and $\Delta\eta = \eta(B) - \eta(B = 0)$. Determining the complex Faraday angle $\Delta\Theta_F(\omega, B)$ is important for studies of the OQHE, as the transverse magnetoconductivity can be readily determined from:



$$\Delta\Theta_F(\omega, B) = \Delta\theta_F(\omega, B) + i\Delta\eta(\omega, B) = \frac{Z_0}{2n}\sigma_{xy}(\omega, B), \quad (1)$$

where n is the refractive index of the material sandwiching the confined carriers and $Z_0 = 377 \Omega$. Hence, the ellipticity change $\Delta\eta$ corresponds to the imaginary part of σ_{xy} , and $\Delta\theta_F$ to the real part of σ_{xy} .

In figures 1(d)–(f) the ellipticity change $\Delta\eta$ is shown for all samples in the magnetic field range 0–7.4 T. For the GaAs sample (figure 1(d)) the resonance with frequency proportional to B and $\Delta\eta < 0$ is ascribed to the CR of the 2DEG. The blue branch (above 1 THz frequency) corresponds to hydrogenic $1s-2p^+$ transitions of donor-bound electrons in the n-type substrate, while the red region results from hydrogenic $1s-2p^-$ transitions [23]. These contributions have opposite ellipticity because the B -field lifts the degeneracy of the $2p$ excited states for donor-bound electrons in the substrate. In figures 1(e) and (f), the positive $\Delta\eta$ is assigned to the CRs of the 2DHG within the Ge quantum well. The opposite sign with respect to that for the GaAs 2DEG shows that holes are the dominant charge carrier in the sGe-QWs. The HH valence band of strained Ge is non-parabolic, and the Zeeman effect results in spin-split CRs at high B , while at all B the Rashba interaction can split spin-up to spin-up and spin-down to spin-down CR energies [4, 11, 24].

Carrier density and effective mass

In order to know the magnetic field at which to expect quantum Hall plateaux the carrier density ρ_{2D} of the 2DHG was found accurately. In this section we describe two methods to obtain ρ_{2D} from THz-TDS. Firstly, the experimental longitudinal conductivity $\sigma_{xx} = \sigma'_{xx} + i\sigma''_{xx}$ was obtained from the transmission $T_{xx}(B, \omega) = E_{xx}(B, \omega)/E_{xx}(0, \omega)$ using $\sigma_{xx} = 2n/Z_0(1/T_{xx} - 1)$, where E_{xx} is the transmitted THz field along x for an incident pulse along x [25]. The real part of σ_{xx} was then used to determine the sheet density via the sum rule: [26]

$$\rho_{2D}^{\text{sum}} = \frac{2m_{\text{THz}}^*}{\pi e^2} \int_{f_1}^{f_2} d\omega \sigma'_{xx}(\omega). \quad (2)$$

Here, m_{THz}^* is an estimate of the effective mass given by a linear fit to the CR frequencies for $B \leq 3$ T. The frequency interval (f_1, f_2) can be varied to match a particular transition, for instance as required to isolate the

Table 1. Sheet carrier density evaluated from: equation (2) (ρ_{2D}^{sum}); fits of time and frequency domain data (ρ_{2D}^{THz}); classical Hall conductivity (ρ_{2D}^{Hall}). Effective mass from: linear fit of CRs (m_{THz}^*); fits of the CR transition energies (m_b^*). The transport lifetime τ_{tr} was used to get the mobility $\mu = e\tau_{\text{tr}}/m_b^*$.

	ρ_{2D}^{sum} (10^{11} cm^{-2})	ρ_{2D}^{THz} (10^{11} cm^{-2})	ρ_{2D}^{Hall} (10^{11} cm^{-2})	m_{THz}^* (m_0)	m_b^* (m_0)	τ_{tr} (ps)	μ ($10^6 \text{ cm}^2 \text{ V}^{-1} \text{ s}^{-1}$)
Ge-10nm	13.0 ± 0.2	13.3 ± 0.5	13.5 ± 0.4	0.12 ± 0.001	0.091 ± 0.001	75 ± 4	1.45 ± 0.08
Ge-20nm	12.5 ± 0.2	12.3 ± 0.3	13.1 ± 0.4	0.11 ± 0.001	0.091 ± 0.001	79 ± 3	1.52 ± 0.06

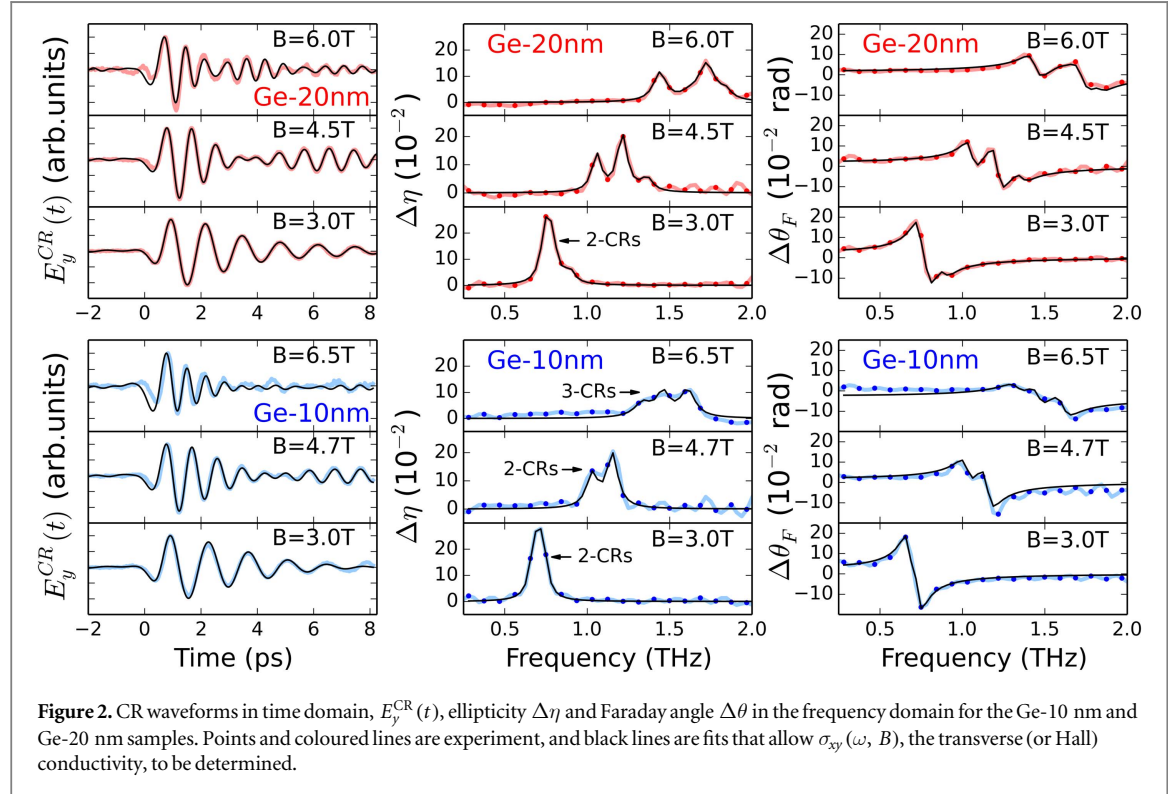


Figure 2. CR waveforms in time domain, $E_y^{\text{CR}}(t)$, ellipticity $\Delta\eta$ and Faraday angle $\Delta\theta$ in the frequency domain for the Ge-10 nm and Ge-20 nm samples. Points and coloured lines are experiment, and black lines are fits that allow $\sigma_{xy}(\omega, B)$, the transverse (or Hall) conductivity, to be determined.

2DEG response of the GaAs/AlGaAs sample from the hydrogenic transitions in the substrate. For this sample, the obtained effective mass was $0.069 m_0$, and the electron density was $4.4 \times 10^{11} \text{ cm}^{-2}$, in excellent agreement with device magnetotransport measurements [16], validating this procedure. Hole sheet densities within the Ge-QWs were averaged for data in the magnetic field range without well resolved split-CRs ($B \leq 3.5 \text{ T}$). The obtained values of m_{THz}^* and ρ_{2D}^{sum} are reported in table 1: the masses are similar, and the densities are comparable.

The sheet density can be alternatively evaluated, together with the CR-frequencies and lifetimes, by fitting $\Delta\theta_F$ and $\Delta\eta$, which are linked to the real and imaginary parts of $\sigma_{xy}(\omega)$ [13, 21]. Here, the Drude–Lorentz transverse magnetoconductivity was assumed [27], given by $\sigma_{xy}(\omega) = \sum_i A_i (\omega_{c,i} / ((\omega + i/\tau_i)^2 - \omega_{c,i}^2))$, where the \sum_i considers different CR-transitions having angular frequencies $\omega_{c,i}$ and lifetime τ_i . The i th amplitude is given by $A_i = \rho_{2D,i} e^2 / m_i^*$, where e is the carrier charge, m_i^* the cyclotron mass (from $m_i^* = eB / \omega_{c,i}$) and $\rho_{2D,i}$ is the sheet density involved in the i th CR. Parameters from frequency-domain fits were validated by time-domain fits [4, 28], which can for instance give more accurate lifetimes if experimental time windows are comparable to τ_i .

Fits to $\Delta\eta$ for the GaAs 2DEG’s CR (figure 1(d)) used $n = 3.6$ in equation (1). As a proof of the reliability of the adopted model, an electron density of $\rho_{2D} = 4.5 \times 10^{11} \text{ cm}^{-2}$ per quantum well was found, in good accord with the sum-rule result above. In figure 2, the experimental CRs in the time domain for the sGe-QWs, together with $\Delta\eta$ and $\Delta\theta_F$ (coloured lines) and fits (black lines) using $n = 3.8$ [29], are shown at various B . The total sheet density for the Ge samples, ρ_{2D}^{THz} , averaged in the magnetic field range $1.5 \leq B \leq 3.5 \text{ T}$, is in line with ρ_{2D}^{sum} , as reported in table 1.

A different evolution of the CRs with B is observable by comparing the Ge-20 nm and Ge-10 nm samples. At $B = 3.0 \text{ T}$ the ellipticity $\Delta\eta$ of the 20 nm well displays a prominent shoulder at high frequency. This appears for $B > 2.0 \text{ T}$ and is still present at 4.5 T where $\Delta\eta$ consists of three resonances. On the other hand, the Ge-10 nm sample exhibits a transition from one to two clearly resolved CRs at 4.7 T evolving into three CRs for $B \geq 6.4 \text{ T}$.

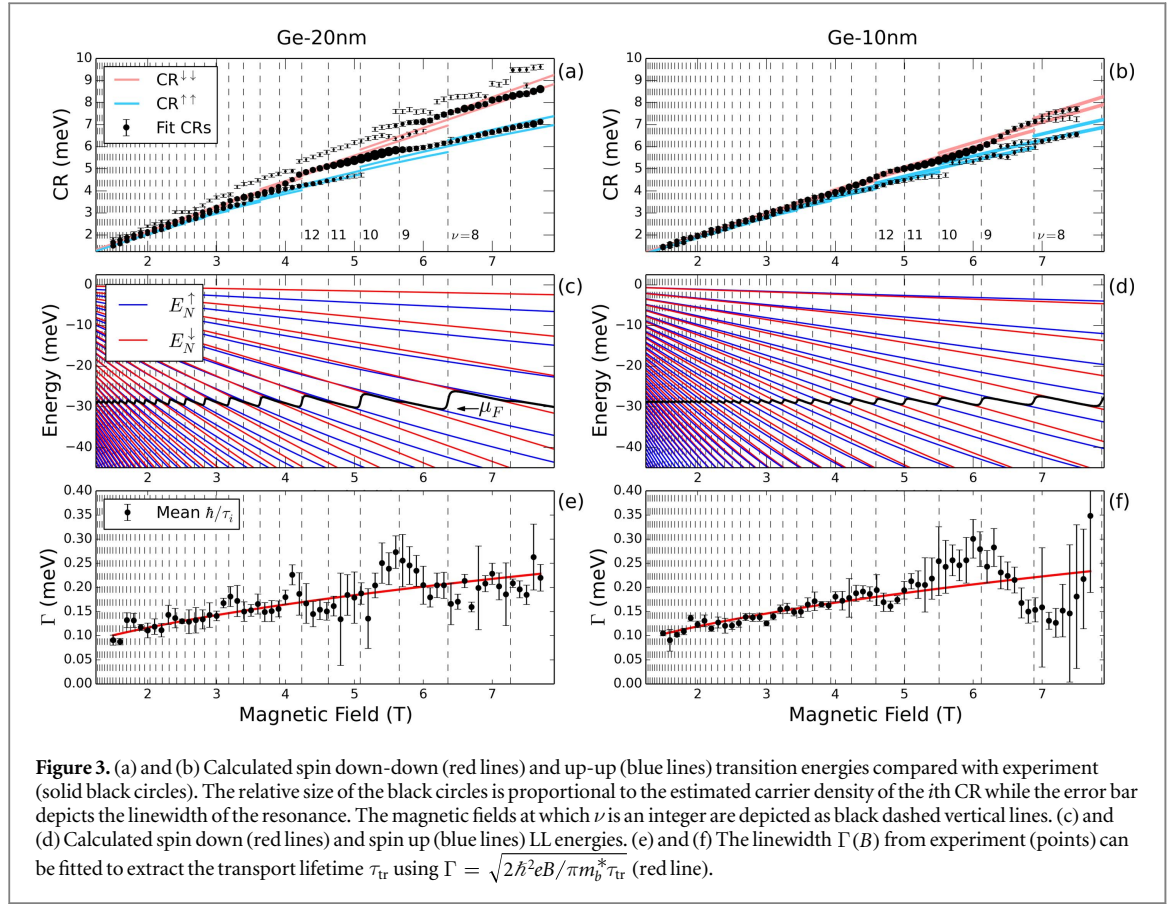


Figure 3. (a) and (b) Calculated spin down-down (red lines) and up-up (blue lines) transition energies compared with experiment (solid black circles). The relative size of the black circles is proportional to the estimated carrier density of the i th CR while the error bar depicts the linewidth of the resonance. The magnetic fields at which ν is an integer are depicted as black dashed vertical lines. (c) and (d) Calculated spin down (red lines) and spin up (blue lines) LL energies. (e) and (f) The linewidth $\Gamma(B)$ from experiment (points) can be fitted to extract the transport lifetime τ_{tr} using $\Gamma = \sqrt{2\hbar^2 eB / \pi m_b^* \tau_{tr}}$ (red line).

As the hole masses and densities are similar (table 1) this implies that another material parameter differs between samples. In the following we examine whether the Zeeman or the Rashba energies drive these differences.

Zeeman and Rashba energies

To investigate further, the CR-energies from fits are reported as black circles in figures 3(a) and (b). Landau fans, reported in figures 3(c) and (d) for spin up (blue lines) and spin down (red) levels, were calculated in order to model the experimental CR energies, using the approach detailed in [4]. This includes the influence of the Rashba effect, through the splitting energy Δ , and the Zeeman effect (proportional to the g -factor). The energy dependence of the effective mass and g -factor due to non-parabolicity was considered using $m^* = m_b^*(1 + 2E/E_g)$ and $g^* = g_0^*(1 - \alpha_{NP}E)$, respectively [30]. Here, m_b^* is the Γ -point effective mass, E_g is the energy gap of Ge and α_{NP} is a non-parabolicity factor. The chemical potential μ_F (black lines in figures 3(c) and (d)) jumps between different LL energies E_N when ν is an integer, at values of B (vertical dashed lines) obtained considering $B = \hbar\rho_{2D}/e\nu$ with $\rho_{2D} = \rho_{2D}^{THz}$. CRs appear and disappear at integer filling ν , owing to the evolution of the LL occupancy.

The energy of the strongest transitions in experiment (big black circles) are in agreement with the spin-down-down (CR $^{\downarrow\downarrow}$, red lines) and spin-up-up (CR $^{\uparrow\uparrow}$, blue lines) transition energies between spin-split LLs. Note that, for simplicity, we assumed δ -function LLs (width $\Gamma = 0$) in the Landau fan calculation, i.e. neglecting disorder [31]. For this reason, two CR $^{\downarrow\downarrow}$ and two CR $^{\uparrow\uparrow}$ are considered in the model because Γ may result in an overlap between the last two occupied LLs, giving rise to up to four CRs (as discussed later with regard to figure 5). The model will also underestimate the CR energy when the uppermost LL is more than half occupied as it does not include the JDOS; the LLs broadening is investigated later in the text.

The best agreement of the model with the experimental CRs energies was obtained with $\Delta = 0.4 \pm 0.2$ meV and $m_b^* = 0.091 \pm 0.001 m_0$ for both samples. Previously we found $\Delta \simeq 2.0$ meV and $m_b^* = 0.103 m_0$ for a Ge-QW with 0.8% strain and a similar sheet density ($9.7 \times 10^{11} \text{ cm}^{-2}$) [4]. Since the strain increases $E_{HH,LH}$ (the HH-LH band energy difference at the Γ point) and $\Delta \propto 1/(E_{HH,LH})^2$, the lower values reported in the current work agrees with the expectation that Δ decreases with strain [2, 4, 9]. The modelled g -factors were $g_0^* = 2.8 \pm 0.5$ and 5.0 ± 0.5 for the Ge-10 nm and Ge-20 nm samples, respectively, with a non-parabolicity constant $\alpha_{NP} = 0.025 \pm 0.005 \text{ meV}^{-1}$. As the Zeeman splitting is proportional to the g -factor, sample Ge-20 nm has a larger Zeeman energy than Ge-10 nm, with consequences for the OQHE plateaux reported later in the manuscript.

For 0.8% strained Ge-QWs with thickness 11 nm and 22 nm we found previously that $g_0 = 3.2$ and 7.0 , respectively [4].

The small size of the Rashba energy ($\Delta = 0.4$ meV) in the present case results in a small contribution to the CR splitting of < 0.1 meV (as assessed by a comparison of the Landau fan with and without Δ), and which is independent of B .

Mobility

To verify that the sGe-QWs studied have sufficiently high mobility to enter the quantum Hall regime, the transport mobility was determined from the B -dependence of the CR linewidth $\Gamma = \hbar / \tau_{\text{THz}}$. Here, τ_{THz} is the average of the different τ_i obtained by fitting $\Delta\eta$, $\Delta\theta_F$ and $E_y^{\text{CR}}(t)$. $\Gamma(B)$ is shown in figures 3(e) and (f) for Ge-10 nm and Ge-20 nm. The overall magnetic field evolution of Γ is consistent with $\Gamma \propto \sqrt{B}$, as expected when the mobility is mainly affected by a short-range scattering potential [32]. The fit of this dependence, shown as the red line, allows the extrapolation of the transport lifetime τ_{tr} and mobility [4]. We estimate $\tau_{\text{tr}} = 75 \pm 4$ ps and 79 ± 3 ps for the Ge-10 nm and Ge-20 nm samples, with mobilities $\mu = e\tau_{\text{tr}}/m_b^* = (1.45 \pm 0.08) \times 10^6 \text{ cm}^2 \text{ V}^{-1} \text{ s}^{-1}$ and $(1.52 \pm 0.06) \times 10^6 \text{ cm}^2 \text{ V}^{-1} \text{ s}^{-1}$ respectively. The higher mobility than our previous report of $\mu \sim 6 \times 10^5 \text{ cm}^2 \text{ V}^{-1} \text{ s}^{-1}$ ($\tau_{\text{tr}} \sim 30$ ps) for 0.8% strain may be linked to the larger $E_{\text{HH,LH}}$. The apparent oscillation in τ_{THz} at different filling factors may be related to the variation in LL occupancy [32–34], as the CR linewidth depends on the width of the unoccupied region of the final LL. This point is elucidated in the JDOS description later in the manuscript.

Optical QHE

Given the high mobility and precise knowledge of the filling factor demonstrated above, we examined the transverse magnetoconductivity for signs of the OQHE. We adopted the approach of [12, 13] where σ_{xy} was normalised by the CR response to give $\tilde{\sigma}_{xy}$. Here, $\tilde{\sigma}_{xy}$ acts as an effective density which, for high mobility 2D systems, should show plateaux at integer values of ν similar to those seen in the dc QHE. Conversely, in the classical limit (low B or high ν) a straight line is expected, as $\tilde{\sigma}_{xy} \rightarrow \rho_{2D}h/eB$.

The evolution of $\tilde{\sigma}_{xy}$, obtained from the fits of $\sigma_{xy}(\omega, B)$, is shown in figure 5 for both Ge-QWs (solid circles). The classical limit is also shown (red lines) and was obtained using the sheet densities $\rho_{2D}^{\text{Hall}} = 13.5 \pm 0.4 \times 10^{11} \text{ cm}^{-2}$ for Ge-10 nm and $13.1 \pm 0.4 \times 10^{11} \text{ cm}^{-2}$ for Ge-20 nm. As can be seen in table 1, these densities are in good accord with those from the sum-rule method and from fitting $\Delta\eta$ and $\Delta\theta_F$. In the limit of smaller ν (larger B) clear plateaux are evident in $\tilde{\sigma}_{xy}$ for both samples at even filling factors $\nu = 10, 12$ and 14 . In particular, these appear wider for the Ge-20 nm sample while for the Ge-10 nm a clear plateaux is resolved at the odd filling factor $\nu = 11$.

The observation of an OQHE plateaux at odd filling factor $\nu = 11$ implies that there is substantial spin splitting: in the absence of spin splitting the spin up and down states are degenerate and plateaux are at even ν [4]. For instance, for a gated GaAs 2DEG the OQHE around odd values of ν was attributed to the Zeeman effect [14]. Here, the relative weakness of the Rashba spin-splitting term suggests that the Zeeman term is responsible for the plateaux at $\nu = 11$ in Ge-10 nm. The insets in figure 4 show the evolution of μ_F and the LL energies with the filling factor for both samples. A plateaux in σ_{xy} arises when μ_F lies inbetween two LLs, where changing B does not change the density of occupied states. Note that for Ge-10 nm, the LLs are well spaced in energy and ν , and hence on sweeping ν via changing B (as in the experiment) plateaux in σ_{xy} may be resolved at odd or even ν . However for Ge-20 nm the larger effective g -factor g_0^* has modified the LL dispersion, and odd and even levels are close together (within the LL linewidth, see next section). This may explain the lack of odd plateaux in the experimental result for Ge-20 nm: while there is a well defined jump in μ_F for even ν , the change is less pronounced for odd ν and the plateaux should be correspondingly weaker, or narrower in B .

The width $\Delta\nu$ of the OQHE plateaux reported in figure 4 in terms of the filling factor ν is $\Delta\nu \sim 0.5$ for all the plateaux observed between $\nu = 10$ and $\nu = 14$. This is relatively large in comparison to the OQHE plateaux widths reported for high mobility 2DEGs [13, 14]. Ikebe *et al* reported that $\Delta\nu \sim 0.05 \rightarrow 0.1$ for the THz OQHE around $\nu = 2$, while the dc Hall plateaux were broader ($\Delta\nu \sim 0.4$) [13]. Similarly, Stier *et al* found that $\Delta\nu \sim 0.1$ for OQHE plateaux in the Faraday angle (around $\nu = 4$), with wider dc plateaux [14]. The difference between the dc and OQHE plateaux width was assigned by Ikebe *et al* to the difference in length scales probed by dc Hall measurements and ac THz spectroscopy [13]. A number of factors may contribute to the larger $\Delta\nu$ reported here: the OQHE plateaux width depends on factors that include the distance travelled by a carrier in one oscillation period of the THz electric field, the characteristic length scale of disorder, and the LL index [13]. A comparison to the dc plateaux widths was not possible for devices made on these samples, although QHE plateaux have been seen in similar sGe QWs [3, 7, 8].

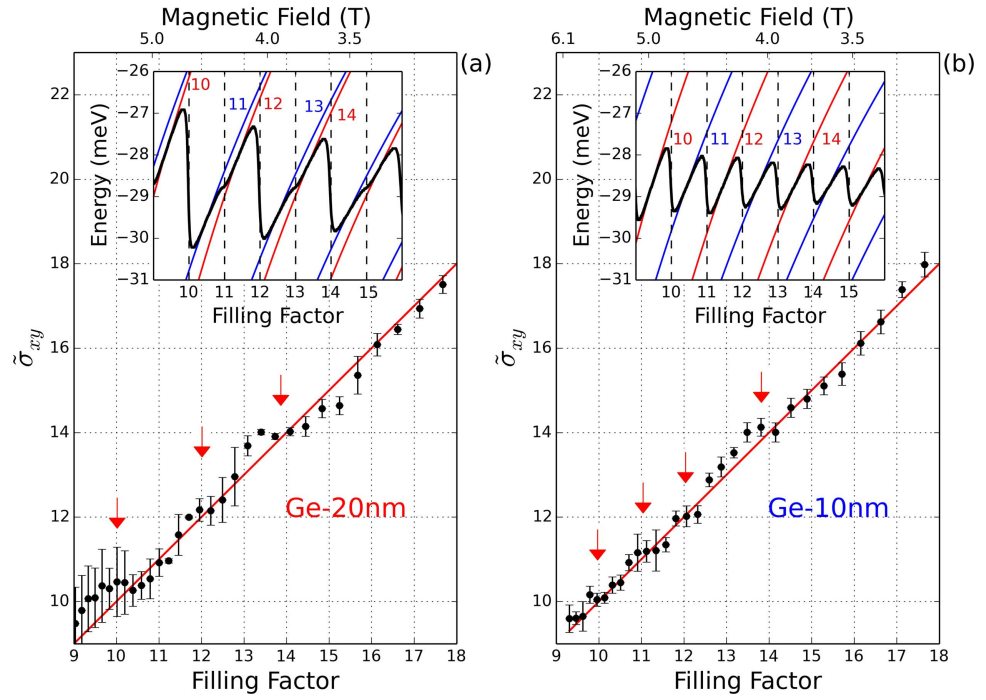


Figure 4. Normalised optical Hall conductivity $\tilde{\sigma}_{xy}$ as a function of filling factor and magnetic field (solid circles). At integer fill factors σ_{xy} shows evident deviations from the Drude classical limit (red lines), with plateaux around $\nu = 10, 12, 14$ (Ge-20 nm) and $\nu = 10, 11, 12, 14$ (Ge-10 nm). The insets show the evolution of the chemical potential (black line) and LLs (blue and red lines) with the filling factor.

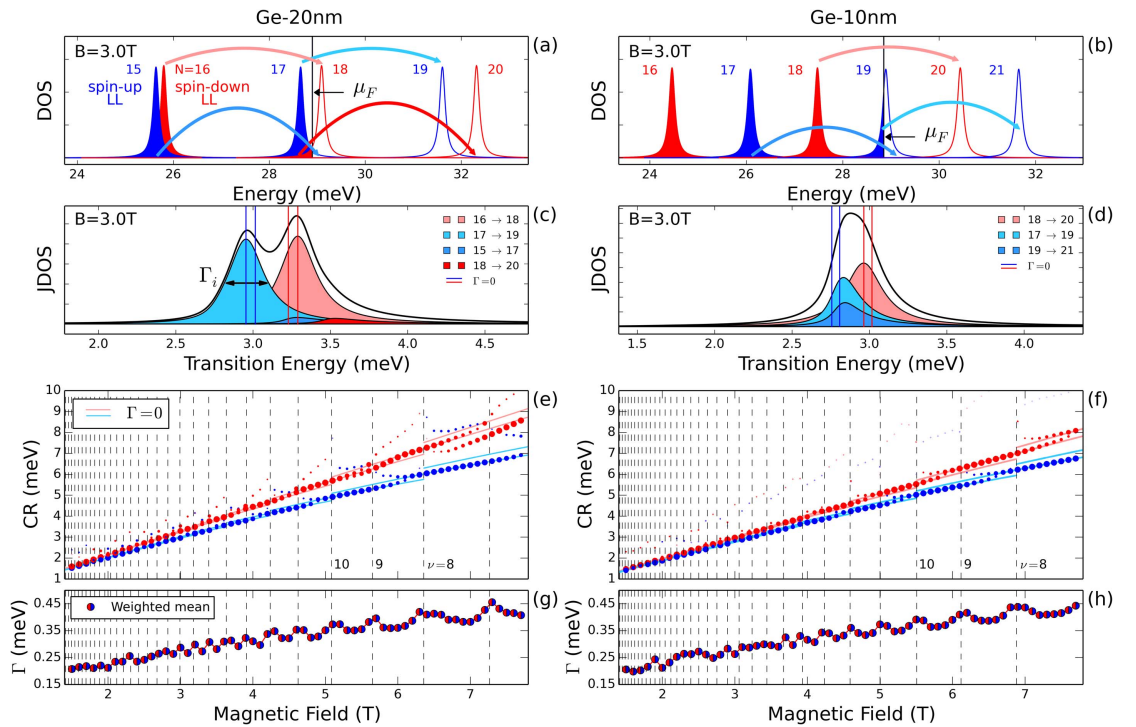


Figure 5. (a) and (b) Density of states (DOS) of LLs at $B = 3.0$ T assuming a Lorentzian shape. Arrows mark spin-conserving transitions between occupied and unoccupied LLs. (c) and (d) Joint DOS at $B = 3.0$ T for the transitions in (a) and (b). The black line shows the total JDOS, while the shaded areas denote the contributions from individual transitions with different widths Γ_i . (e) and (f) Evolution with B of the transition energies given by the maximum of the JDOS peaks. The dot size represents the amplitude of the different contributions. Red and blue lines depict the $\Gamma = 0$ transition energies. (g) and (h) Evolution with B of the mean of Γ_i , weighted by the peak intensities. Maxima appear at integer ν .

Joint density of states

To qualitatively clarify the oscillation of Γ with B (figures 3(e) and (f)) and the differences between the two samples, the JDOS was calculated from the LL fans in figures 3(c) and (d). LLs with a Lorentzian shape were assumed, with a width given by the fitted $\Gamma(B) \propto \sqrt{B}$ (red lines in figures 3(e) and (f)). A comparison between the DOS for the two samples at $B = 3$ T is given in figures 5(a) and (b). Adjacent odd and even LLs for Ge-20 nm overlap and, when μ_F crosses two adjacent LLs, four spin-conserving CR transitions are therefore allowed (arrows in figure 5(a)). A negligible overlap results for the Ge-10 nm sample in figures 5(b) where, depending on the position of μ_F , only two or three (pictured) CRs can appear. The shaded areas in figures 5(c) and (d) show the JDOS contribution for each transition. The optical conductivity is proportional to the JDOS (black line), and can therefore exhibit shoulders or non-Lorentzian lineshapes as a result of partial LL occupancy. The two small contributions in figure 5(c) as well as the two spin-up to spin-up transitions in figure 5(d) (blue areas), differ in transition energy from the $\Gamma = 0$ case (blue and red vertical lines). The calculated JDOS in figures 5(c) and (d) can be qualitatively compared with the experimental ellipticity reported in figure 2. While two CRs are resolved in the experimental ellipticity at $B = 3.0$ T for Ge-20 nm, only one is resolved for Ge-10 nm, as in the JDOS model.

The overall trend at different B is depicted in figures 5(e) and (f), which can be compared with figures 3(a) and (b). Note that for Ge-20 nm, with larger g_0^* , the JDOS of the relatively weak, higher CR energy transitions is greater than that for Ge-10 nm, in agreement with experiment. Finally, figures 5(g) and (h) illustrates the mean linewidth Γ from the JDOS calculation (where each CR's contribution is weighted by its amplitude) at different B . The oscillation evident in Γ present maxima at integer filling factor and minima at half-integer ν . The JDOS is narrowest when the uppermost LL is half-full, at half-integer ν . This gives a qualitative explanation for the oscillation in $\Gamma(B)$ from experiment reported in figures 3(e) and (f).

Conclusion

In summary, the longitudinal and transverse magnetoconductivity of strained Ge quantum wells has been characterized, in a non-contact manner, by means of polarisation-resolved THz-TDS. An improved mobility, but a lower spin-splitting energy, was found in comparison to Ge-QWs with lower strain. By determining the off-diagonal component of the conductivity tensor experimentally the OQHE at terahertz frequencies was observed for spin-split HHs states, apparent as plateaux-like structures in the normalised σ_{xy} . Samples with different well width resulted in qualitatively different OQHE features, as a result of the suppressed g -factor in narrow quantum wells changing the Zeeman energy. This work expands the number of material systems known to exhibit the OQHE, and suggests a promising future for strained Ge in fundamental and applied physics. It is also important to undertake further experimental and theoretical studies of the OQHE to understand how localised and delocalised states contribute.

Acknowledgements

The authors would like to acknowledge funding from the EPSRC (UK, project EP/J003263/1 'Spintronic device physics in Si/Ge Heterostructures') and the ERC (Advanced Grant, 'Quantum Metamaterials in the Ultra Strong Coupling Regime').

References

- [1] Manchon A, Koo H C, Nitta J, Frolov S M and Duine R A 2015 *Nat. Mater.* **14** 871
- [2] Moriya R *et al* 2014 *Phys. Rev. Lett.* **113** 086601
- [3] Morrison C, Myronov M, Wiśniewski P, Rhead S D, Foronda J and Leadley D R 2014 *Appl. Phys. Lett.* **105** 182401
- [4] Failla M, Myronov M, Morrison C, Leadley D R and Lloyd-Hughes J 2015 *Phys. Rev. B* **92** 045303
- [5] Dobbie A, Myronov M, Morris R J H, Hassan A H A, Prest M J, Shah V A, Parker E H C, Whall T E and Leadley D R 2012 *Appl. Phys. Lett.* **101** 172108
- [6] Myronov M, Morrison C, Halpin J, Rhead S, Foronda J and Leadley D 2015 *Solid-State Electron.* **110** 35
- [7] Shi Q, Zudov M A, Morrison C and Myronov M 2015 *Phys. Rev. B* **91** 241303
- [8] Mironov O A, D'Ambrumenil N, Dobbie A, Leadley D R, Suslov A V and Green E 2016 *Phys. Rev. Lett.* **116** 176802
- [9] Fischetti M V and Laux S E 1996 *J. Appl. Phys.* **80** 2234
- [10] Schäffler F 1997 *Semicond. Sci. Technol.* **12** 1515
- [11] Winkler R 2003 *Spin-Orbit Coupling Effects in Two-Dimensional Electron and Hole Systems* (Berlin: Springer)
- [12] Morimoto T, Hatsugai Y and Aoki H 2009 *Phys. Rev. Lett.* **103** 116803
- [13] Ikebe Y, Morimoto T, Masutomi R, Okamoto T, Aoki H and Shimano R 2010 *Phys. Rev. Lett.* **104** 256802
- [14] Stier A V *et al* 2015 *Phys. Rev. Lett.* **115** 247401
- [15] Shimano R, Yumoto G, Yoo J Y, Matsunaga R, Tanabe S, Hibino H, Morimoto T and Aoki H 2013 *Nat. Commun.* **4** 1841

- [16] Maissen C, Scalari G, Valmorra F, Beck M, Faist J, Cibella S, Leoni R, Reichl C, Charpentier C and Wegscheider W 2014 *Phys. Rev. B* **90** 205309
- [17] van der Valk N C, van der Marel W A and Planken P C 2005 *Opt. Lett.* **30** 2802
- [18] Lloyd-Hughes J, Jones S P P, Castro-Camus E, Doig K I and MacManus-Driscoll J L 2014 *Opt. Lett.* **39** 1121
- [19] Arikawa T, Zhang Q, Ren L, Belyanin A A and Kono J 2013 *J. Infrared Millim. Terahertz Waves* **34** 724
- [20] Akhiezer A I 1975 *Plasma Electrodynamics* (Oxford: Pergamon)
- [21] O'Connell R F and Wallace G 1982 *Phys. Rev. B* **26** 2231
- [22] Palik E D and Furdyna J K 1970 *Rep. Prog. Phys.* **33** 1193
- [23] Lloyd-Hughes J, Beere H E, Ritchie D A and Johnston M B 2008 *Phys. Rev. B* **77** 125322
- [24] Engelhardt C M, Többen D, Aschauer M, Schäffler F, Abstreiter G and Gornik E 1994 *Solid-State Electron.* **37** 949
- [25] Wang X, Hilton D J, Ren L, Mittleman D M, Kono J and Reno J L 2007 *Opt. Lett.* **32** 1845
- [26] Drew H D and Coleman P 1997 *Phys. Rev. Lett.* **78** 1572
- [27] Lloyd-Hughes J 2014 *J. Phys. D: Appl. Phys.* **47** 374006
- [28] Some D and Nurmikko A V 1994 *Appl. Phys. Lett.* **65** 3377
- [29] Levinstein M E, Rumyantsev S L and Shur M 2001 *Properties of Advanced Semiconductor Materials: GaN, AlN, InN, BN, SiC, SiGe* (New York: Wiley)
- [30] Scriba J, Wixforth A, Kotthaus J P, Bolognesi C, Nguyen C and Kroemer H 1993 *Solid State Commun.* **86** 633
- [31] Davies J H 1998 *The Physics of Low-Dimensional Semiconductors: An Introduction* (Cambridge: Cambridge University Press) <http://loc.gov/catdir/toc/cam024/97000088.html>
- [32] Ando T, Fowler A B and Stern F 1982 *Rev. Mod. Phys.* **54** 437
- [33] Englert Th, Maan J C, Uihlein Ch, Tsui D C and Gossard A C 1983 *Solid State Commun.* **46** 545
- [34] Kamaraju N, Pan W, Ekenberg U, Gvozdi D M, Boubanga-Tombet S, Upadhyaya P C, Reno J, Taylor A J and Prasankumar R P 2015 *Appl. Phys. Lett.* **106** 031902